Deep Learning in Spaceborne GNSS Reflectometry: Correcting Precipitation Effects on Wind Speed Products

Tianqi Xiao, *Student Member, IEEE*, Caroline Arnold, Daixin Zhao, Lichao Mou, Jens Wickert, and Milad Asgarimehr

***Abstract*—Deep learning techniques have shown the capability in GNSS reflectometry (GNSS-R) for retrieving geographical parameters based on GNSS-R observations. Recent studies have proved that such data-driven approaches can significantly improve the quality of ocean surface wind speed products retrieved from delay-Doppler Maps. However, based on the theoretical knowledge, several known error sources are associated with bias in the deep learning model estimations. Rain splashing on the ocean affects the surface roughness of the ocean, altering the scattering pattern of GNSS signals and consequently bringing in considerable bias in wind speed estimations. Correction of such bias is challenging because of its nonlinear dependence on different environmental and technical parameters. Deep learning has the potential to learn such trends from corresponding environmental parameters and correct the associated biases. Therefore, we investigate how deep learning-based data fusion using precipitation data can correct the rain effect and improve wind speed estimations. Our proposed fusion model outperforms both the baseline model and the operational Minimum Variance Estimator (MVE) method on unseen dataset. The root mean square error (RMSE) of our fusion model is 3.3% better than the baseline model and 30% better than the MVE method. For samples affected by rain, our fusion model also shows superior performance compared to the baseline model. Specifically, the retrieval RMSE of the fusion model is improved by 1.9% overall, with a 3.6% improvement in the low wind speed range (<4 m/s) and a 17% improvement in the high wind speed range (>16 m/s).**

***Index Terms*—Deep learning, GNSS reflectometry, ocean wind speed, precipitation.**

I. Introduction

The ocean surface wind has a great impact on the interaction of heat, particulates, gas, and moisture between air and sea, formulation of waves and currents, ocean circulation, as well as development and intensification of extreme climate events. Many human activities, such as fisheries management, navy search and rescue operations, and ship routing, are affected by ocean wind [1], [2], [3]. Conventional in-situ ocean surface wind speed measurements obtained by mechanical anemometer installed on platforms such as ships and buoys are accurate and near continuous, but with limited coverage [2]. Conventional scatterometers and synthetic aperture radar (SAR) are capable of retrieving and monitoring the ocean surface wind speed with a global coverage and their wavelength is long enough to penetrate raindrops and clouds [4], [5], [6]. However, these systems have drawbacks such as large weight and power demands, complexity, and high costs. In addition, their temporal resolution is limited, and they exhibit higher data latency [7].

Spaceborne Global Navigation Satellite System Reflectometry (GNSS-R) is defined as the exploitation of pre-existing signals transmitted by Global Navigation Satellite System (GNSS) after reflection off the Earth surface [8]. As GNSS signals are already globally available with dense coverage, adequate temporal resolution, and high transmissivity in rainy atmosphere [9], [10], GNSS-R satellites require only small, low-power, and low-cost receivers. These receivers track multiple reflected GNSS signals simultaneously onboard low earth orbit (LEO) satellites, thus reducing the development costs while retaining the high sampling frequency and spatial coverage. Several missions have been successfully deployed for observing reflected GNSS signals recently, such as the TechDemoSat-1 (TDS-1) [11], the Cyclone GNSS (CYGNSS) [12], and the Bufeng-1A/B [13], providing large amounts of observations. Many previous studies have been done for ocean wind speed retrieval using the delay-Doppler Map (DDM) captured by the GNSS-R satellites [14], [15], [16], [17]. However, the

Received 27 June 2024; accepted 19 August 2024. Date of publication 3 September 2024; date of current version 11 October 2024. The work of C. Arnold was supported by Helmholtz Association's Initiative and Networking Fund through Helmholtz AI under Grant ZT-I-PF-5-01. This work was supported by Helmholtz AI project AI4GNSSR under Grant ZT-I-PF-5-091 and was supported by the Helmholtz Association's Initiative and Networking Fund on the under Grant HAICORE@FZJ partition. *(Corresponding author: Tianqi Xiao.)*

Tianqi Xiao is with the German Research Centre for Geosciences, 14473 Potsdam, Germany, and also with the Institute of Geodesy and Geoinformation Science, Technische Universität Berlin, 10623 Berlin, Germany (e-mail: xiaotq@gfz-potsdam.de).

Caroline Arnold is with German Climate Computing Center, 20355 Hamburg, Germany (e-mail: anorld@dkrz.de).

Daixin Zhao is with the Data Science in Earth Observation, Technical University of Munich, 80333 Munich, Germany, and also with Remote Sensing Technology Institute, German Aerospace Center, 82234 Wessling, Germany (e-mail: daixin.zhao@tum.de).

Lichao Mou is with the Data Science in Earth Observation, Technical University of Munich, 80333 Munich, Germany (e-mail: lichao.mou@tum.de).

Jens Wickert is with the German Research Centre for Geosciences, 14473 Potsdam, Germany, and also with the Institute of Geodesy and Geoinformation Science, Technische Universität Berlin, 10623 Berlin, Germany (e-mail: wickert@gfz-potsdam.de).

Milad Asgarimehr is with the Institute of Geodesy and Geoinformation Science, Technische Universität Berlin, 10623 Berlin, Germany, and with the Department of Signal Theory and Communications, Universitat Politecnica de Catalunya, 08034 Barcelona, Spain, and also with the German Research Centre for Geosciences, 14473 Potsdam, Germany (e-mail: milad.asgarimehr@gfz-potsdam.de).

Digital Object Identifier 10.1109/JSTARS.2024.3453999

information contained in DDM is only partly used by most of the studies as parameters derived from the partial matrix.

With the development of Artificial Intelligence (AI), data-driven approaches have become increasingly popular in the field of remote sensing [18], [19]. The accumulating GNSS-R datasets provide the opportunity for the application of such techniques. In [20], a feed-forward artificial neural network (ANN) with one hidden layer was proposed using TDS-1 observations including both scientific and technical parameters. The model showed an improvement of 20% in the root mean square error (RMSE) compared to a least square-based retrieving approach. A more complex multilayer perceptron (MLP) network was proposed in [21] using simulated CYGNSS observables. The entire DDM over a specified window was utilized to preserve all possible information in the raw observations. The model was also tested on a real CYGNSS dataset with the overall RMSE of 1.79 m/s for wind speed samples between 3 m/s and 20 m/s. Further in [22], the proposed model output wind speed estimations undergo a cumulative distribution function (CDF) correction to achieve better accuracy, global generalization, and stability in time.

Further, some studies exploited other structures for better model performance, such as long short-term memory (LSTM) and convolutional neural networks (CNNs). Considering the temporal correlation information of features, a hybrid model combining LSTM and attention mechanism was implemented to enhance the quality and efficiency of ocean wind speed retrieval [23]. In order to preserve as much information that DDM contains, a multimodal network for heterogeneous GNSS-R data fusion [21] was proposed to use CNN for processing TDS-1 DDMs and combining other one-dimensional (1-D) features extracted from satellite receiver status parameters using linear layers. However, these studies train their models based on the basic pipeline of data split preparation, which is to split the preprocessed dataset randomly into training, validation, and test split with a certain ratio. Moreover, the entire dataset is usually collected in a very short period, which introduces high temporal dependence within their samples. Therefore, their models may not be well generalized in time and could have an unstable performance in estimating wind speed for future samples. To address the issue mentioned above, CyGNSSnet [24] was proposed along with a preprocessed 15-month CYGNSS dataset consisting of splits according to time span for better performance and generalization. Furthermore, the hybrid CNN-LSTM model was implemented to capture spatiotemporal dependencies between the input DDM sequences [25]. Also, transformer-based models were proposed to estimate the ocean wind speed from another perspective of AI [26], which achieves promising accuracy without using any ancillary information.

However, the aforementioned studies have witnessed a degraded model performance at high wind speeds due to the lack of high wind speed training samples compared to low wind speed samples. The data distribution and quality also differed between these intervals. To address this problem, a few studies proposed to separate high wind samples and process them with individual models [27]. Furthermore, several machine learning models were investigated in [28], and models were trained separately for low and high wind speed samples to improve the accuracy of high wind speed estimation. Although the proposed model achieved better accuracy for high wind speed, it required knowing whether the sample was in the high wind speed interval.

Moreover, geophysical parameters, such as swell, precipitation, and atmospheric pressure, could further degrade the model performances not only at the high wind speed interval but across all wind speed ranges with varying degrees. These effects of geophysical parameters introduce the decorrelation between the observed variations in the received scattered signal and the ocean surface wind field, leading to bias in the data product [29], [30], [31], [32], [33], [34]. The nonlinear dependence of the bias on different environmental and technical parameters remains an obstacle to eliminating such bias. Thus, incorporating data on precipitation and other relevant geophysical parameters into the modeling process can mitigate the impact of these environmental disturbances and can improve the model performance across all wind speed ranges. By integrating these factors, data fusion is proposed in preprocessing steps and as the model inputs. The significant wave height (SWH) caused by swells was used as an extra parameter because GNSS-R signals operating in longer wavelengths are more likely to be influenced by waves less coupled with surface winds [28]. Data fusion with the mean sea level (MSL) pressure was performed in [27] as the MSL has a more considerable impact on typhoon status and track. However, the precipitation may affect the GNSS-R observations in several ways. For instance, the raindrops will form ring waves on the ocean surface, contributing to the overall roughness of the ocean surface, especially in the presence of low wind speed [32]. However, when the wind speed becomes larger, such enhancement from the ring waves becomes less obvious. In addition, rain tends to suppress larger waves, which are usually caused by higher wind speed as the rain intensity increases [35]. However, there are not many studies that focus on correcting the effect of precipitation globally, even if the signature of rain in GNSS-R observables is investigated and discussed in [30], [31], and [32]. The combined effect of SWH, wave direction, and precipitation was considered by the model proposed in [36] with a random split of training and inference data split. The model yields a better estimation but the analysis for the effect of each external parameter is limited. Afterward, a pipeline of joint retrieval of several geophysical parameters was proposed in [37] and assessed by a case study in a limited area. The pipeline requires additional prior knowledge which may not be available during future inference.

Herein our study emphasizes the precipitation effect on global ocean surface wind speed retrieval using GNSS-R. According to the theoretical model, the scattering mechanism changes during the growth of ocean surface roughness. In the case of weak winds, partially coherent scattering dominates, whereas, in a higher range of wind speeds, the completely noncoherent, strong diffuse scattering takes place [39]. In our study, deep learning-based data fusion is thus proposed to correct the precipitation effects for ocean wind speed products. We investigate the applicability and stability of the deep learning neural network fused with external information and demonstrate the benefits of deep learning-based data fusion in GNSS-R ocean monitoring. We evaluate how much our model utilizing precipitation data in addition to GNSS-R observables can correct the rain effects

TABLE I
MEASUREMENTS USED AS DDMS [38]

Parameter	Unit	Description
raw_counts	1	17 x 11 array of DDM bin raw counts. These are the uncalibrated power values produced by the DDMI.
power_analog	Watt	17 x 11 array of DDM bin analog power. This is the true power that would have been measured by an ideal (analog) power sensor.
brcs	m^2	17 x 11 array of DDM bin bistatic radar cross section. It is generated by unwrapping the forward scattering model.
eff_scatter	m^2	17 x 11 array of DDM bin effective scattering area. It represents the true surface scattering area contributing to each DDM bin. It is calculated by convolving the GPS ambiguity function with the surface area that contributes power to a given DDM bin as determined by its delay and Doppler values and the measurement geometry.

and consequently improve the quality of the ocean wind speed estimates for both moderate and extreme wind speed intervals. In addition, a case study of tracking Hurricane Laura is performed using our fusion model to further evaluate its reliability under extreme weather conditions, which is important for disaster response and mitigation efforts.

In the subsequent sections, we first introduce the dataset used in this study and the preprocessing procedure for the experiments. Then we explain our deep learning model architecture, data fusion experiment setup, and metrics for evaluation in detail. Next, we show evaluation results over the test dataset and compare the model performance. Afterwards, we discuss the impact of the input parameters, and the applicability as well as the potential of our proposed model. Finally, we summarize our study and draw conclusions.

II. DATASET AND PREPROCESSING

Our experiments are carried out based on three datasets, which are CYGNSS Level 1 Science Data Record Version 3.0, global precipitation measurements (GPM) final run data, and ERA5 reanalysis data, starting from August 2018 to April 2021.

CYGNSS Level 1 data are provided by NASA's Physical Oceanography Distributed Active Archive Centre (PO.DAAC) [40]. Eight data files in NetCDF format are provided each day, each corresponding to a unique spacecraft in the CYGNSS constellation.

As the main measurement of the CYGNSS mission, DDMs become the main input of our models. CYGNSS Level 1 data provides four observation variables with the size of 17×11 : raw counts, analog power, effective scattering area, and bistatic radar cross section (BRCS). The detailed description is given in Table I [38].

In addition to DDMs, each sample contains several useful engineering and science measurement parameters related to the DDM, the transmitting satellites, and the measurement geometry. Science measurement parameters, such as NBRCS and LES, are significant for conventional wind speed retrieval approaches. The NBRCS in CYGNSS data is defined as the normalized BRCS value of a 3×5 pixel box which could be used as the delay-Doppler Map average (DDMA); the LES is the slope of the leading edge of the integrated delay waveform (IDW) divided by the effective area. More specific computation of NBRCS and LES is introduced in [41] and [42]. Meanwhile, the engineering parameters such as the GPS effective isotropic radiated power (gps_erip) are potentially correlated with the predicted wind speed, which should be considered in our model. To leverage the model operation cost and efficiency, we perform parameter selection for parameters that may have potential relevance to wind speed estimation based on the previous theoretical information, and evaluate the improvement of model performance after adding each parameter.

To avoid introducing dependencies on the same data source as the labels, we make use of GPM final precipitation L3 product [43]. The integrated multisatellite retrievals for GPM (IMERG) collect and merge all satellite microwave precipitation estimates, microwave-calibrated infrared (IR) satellite estimates as well as the precipitation gauge analysis. The final product is created using monthly gauge data after several runs of the system and provides half-hourly global precipitation with a spatial resolution of $0.1^\circ \times 0.1^\circ$. The precipitation parameter will be fed as an external input in our experiments.

ERA5 reanalysis data provides ocean surface wind speed hourly in a $0.25^\circ \times 0.25^\circ$ grid. The wind speed 10 m above the sea surface is given as vectors with two proportional directions [44]. We calculate the wind speed value from the vectors and employ them as our training label as well as the ground truth of evaluation.

As the spatial-temporal resolution of these datasets is inconsistent, it is necessary to collocate the data according to the timestamp and the specular point position of CYGNSS data. We match the GPM and ERA5 datasets with the CYGNSS product and resample them by the nearest neighbor method. We form our dataset by collecting all matched CYGNSS samples that fall within the same spatial and temporal bins as ERA5 data, maximizing the inclusion of samples affected by precipitation, and samples observed at high wind speed in our dataset.

We form our dataset by keeping all CYGNSS samples in the same ERA5 spatial and temporal bin in order to include all samples with precipitation and/or high wind speed.

Quality control is applied after the collocation to exclude low-quality samples. Poor-quality samples will introduce incorrect intuition and drive the model away from mapping different wind speed labels to their corresponding inputs. Based on [24], we filter the samples by applying rules as follows:

1) The scattering area of NBRCS and LES are valid (not NaN).
2) The uncertainty of the BRCS is lower than 1.
3) The attitude error of the spacecraft is low (quality_flags = 4).

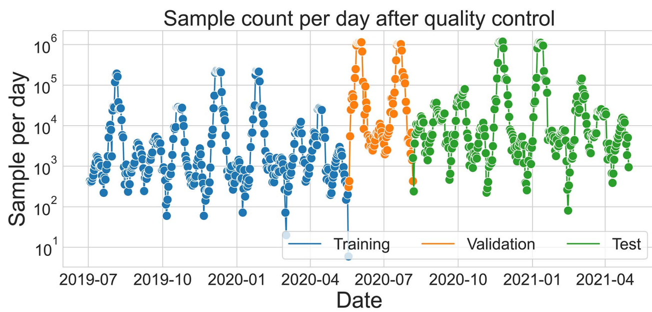

Fig. 1. Data distribution over time of train, validation, and test datasets obtained from CYGNSS Level 1 data after quality control.

4) The nano star tracker attitude status is "OK" (nst_att_status = 0).
5) The range corrected gain (RCG) is larger than 3.
6) The receive antenna gain is larger than 0 dBi.
7) The LES is larger than 0.
8) The Zenith signal-to-noise ratio (SNR) is larger than 0 dB.

Then we exclude 4 365 206 samples lying outside the confidence interval of 95% to reject the outliers caused by fraudulent behavior of GNSS-R instruments or a flaw in ERA5 reanalysis. The major samples could be less affected by unexpected errors. Besides, samples with wind speed labels smaller than 2.5 m/s are not considered because of weak diffuse scattering. The scattering mechanism at winds lower than 2.5 m/s is more like a high-order Bragg scattering instead of quasi-specular forward scattering. Therefore, the DDM-related observables (e.g., NBRCS and LES) become insensitive to low wind speeds due to the change in the scattering mechanism.

After filtering out the low-quality measurements, samples need to be split into three subsets for supervised training, validation, and evaluation, respectively. Since CYGNSS provides data along the observational tracks, the adjacent DDMs in the same track are highly correlated and similar. Random selection of samples for training and test datasets would introduce these correlations that may result in an unconvincing performance analysis on the test dataset, as both training and test samples are picked within the same time interval. Furthermore, operational processing methods are generally based on the existing dataset and then applied to the upcoming data. Hence, we split our data by the acquisition time to verify the performance of our model. The data distribution of each subset is shown in Fig. 1.

We select about 2.9×10^7 samples during 320 days as training data, 1.8×10^7 samples during the next 80 days as validation data, and the remaining 2.1×10^7 samples from the following 266 days as test data, which ensures the model generality and robustness are evaluated with unseen samples.

III. Methodology and Experiments

In order to investigate how deep learning-based data fusion can correct the rain effects, we train two deep learning neural networks: one is trained with external precipitation information, while the other is trained only with the information provided by the CYGNSS Level 1 dataset. The network architecture is fixed after selecting proper ancillary parameters, and thus, the influence of the network architecture is limited in the performance analysis on test datasets. This section will introduce the methodology and explain the setup of our experiments in detail.

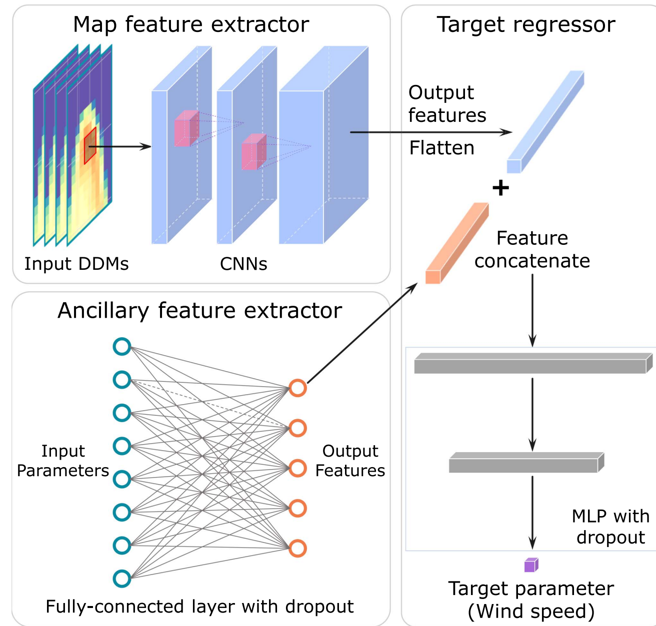

Fig. 2. General structure of CyGNSSnet, modified from [24].

A. Network Architecture

Based on the previous work, we adopt CyGNSSnet and process CYGNSS Level 1 v3.0 data. Our network combines the 2-D DDMs with 1-D variables to extract features directly from the Level 1 sample and predicts the wind speed for each input sample. For a more detailed explanation of CyGNSSnet architecture, please refer to [24]. Fig. 2 outlines the general structure of the network we used in this study.

The network consists of three components: map feature extractor, ancillary feature extractor, and target regressor. The map feature extractor is designed to process 2-D observations such as DDMs. There are various options for extracting features from 2-D inputs. We select CNN as the backbone in this study and add max pooling layers to reduce the number of trainable parameters. The number of convolutional layers, convolution kernels, and pooling layers can be tuned. The ancillary feature extractor processes the other 1-D parameters. We deploy a fully connected (FC) layer to get features and add a dropout layer after it to prevent units from coadapting too much [45]. The wind speed retrieval is done by the target regressor exploiting the features extracted by the previous two components. We use the MLP consisting of FC layers with dropout to retrieve the wind speed. The rectified linear unit (ReLU) function is adopted as the activation function in our network, avoiding the vanishing gradients that occurred in some other activation functions such as sigmoid and tanh [46].

It is important to note that the specific network structure can differ as the number of convolutional layers, and the number and position of the max pooling layers are assigned user-defined arguments. To better compare the model performance on

TABLE II
NUMBER OF IMPROVED MODELS AFTER ADDING EACH PARAMETER

Improved Models Count	Parameter Names
5	gps_eirp, sc_roll, sc_yaw, lna_temp_nadir_port, lna_temp_nadir_starboard, lna_temp_zenith, sp_az_body, sp_az_orbit, sp_rx_gain, sp_theta_body, tx_pos_x, tx_pos_y, tx_pos_z, tx_vel_x, tx_vel_y, tx_vel_z, zenith_sig_i2q2
4	ddm_snr, gps_off_boresight_angle_deg, rx_clk_bias_rate, sp_ddmi_dopp
3	brcs_ddm_peak_bin_delay_row, ddm_noise_floor, brcs_ddm_peak_bin_dopp_col, sp_inc_angle, rx_to_sp_range, sp_theta_orbit, zenith_code_phase
2	brcs_ddm_sp_bin_dopp_col, ddm_brcs_uncert, gps_ant_gain_db_i, gps_tx_power_db_w, inst_gain, les_scatter_area, rx_clk_bias, sc_pitch, sp_fsw_delay
1	brcs_ddm_sp_bin_delay_row, sp_alt, tx_to_sp_range
0	nbrcs_scatter_area, sc_velocity, sp_velocity

correcting rain effects, we set up experiments with the same network structure; details of the experimental setup are described in Section III-C.

B. Parameter Selection

As mentioned in II, engineering and science parameters recorded in the CYGNSS Level 1 dataset also contain potential information for ocean surface wind speed estimation. However, some of the parameters may introduce unexpected dependence and fake correlation to the wind speed estimation and skew the model performance. Therefore, we automatically select ancillary parameters that sufficiently improve the model performance and exclude the less useful ones. The coordinates of specular points are excluded for training in particular to reduce the dependence on location. Initially, NBRCS and LES are selected as the reference since they are commonly exploited in conventional wind speed retrieval algorithms. Then we adopt the preprocessing pipelines in [24] to train five models with different hyperparameter settings separately, adding one single parameter to the reference, and compare the validation loss. Summary of the number of improved models for the additional parameter is reported in Table II.

We encompass those parameters that improve the performance in more than 3 out of 5 models and exclude the others. Our final dataset consisting of all 2-D DDM-like observations and 23 selected ancillary parameters are summarized in Table III.

C. Experiment Setup

The network was implemented with PyTorch Lightning [47] and trained on the server offered by Helmholtz AI computing resources (HAICORE) with an early-stop scheme to reduce the training time. We train two CyGNSSnet models with the same network architecture and different input feature sets. One network processing DDMs plus 23 ancillary parameters provided by the CYGNSS level 1 dataset is the baseline model; the other network exploiting one additional precipitation parameter from

TABLE III
ANCILLARY PARAMETERS PROVIDED BY CYGNSS DATA AS INPUT FEATURES

Type	Name
2D DDM	raw_counts, power_analog, brcs, eff_scatter
DDM Related	ddm_nbrcs, ddm_les, ddm_snr, sp_ddmi_dopp
Transmitter Related	tx_pos_x, tx_pos_y, tx_pos_z, tx_vel_x, tx_vel_y, tx_vel_z
Receiver Related	gps_eirp, sp_rx_gain, lna_temp_zenith, lna_temp_nadir_starboard, lna_temp_nadir_port, rx_clk_bias_rate, zenith_sig_i2q2
Geometry Related	gps_off_boresight_angle_deg, sp_theta_body, sc_roll, sc_yaw, sp_az_body, sp_az_orbit

For detailed descriptions, see CYGNSS L1 V3.0 users's guide and data dictionary [38].

the GPM dataset is the fusion model. Fig. 3 outlines the final network architecture trained for correcting the rain effects. Here, we set a total of 3 convolutional layers. Each layer uses 32 kernels with a window size of 3×3. The padding and stride are set to 1 for each layer, ensuring that the spatial dimensions of the input are preserved throughout the convolutional operations. Batch normalization is done after each convolution. We apply only one maximum pooling layer after the last CNN block with a window size of 2×2. Then the feature maps are flattened into a 1-D vector, resulting in a total of 1280 features. For the FC layers, we set the number of output features for ancillary parameter inputs to $f_0 = 48$ with a dropout rate of 0.01. Subsequently, for the following two FC layers dealing with concatenated feature vectors, we set $f_1 = 4$ with a drop rate of 0.01 and $f_2 = 40$ with a drop rate of 0.09.

Normalization is applied before training to bring all input features into the same scale. We scale each feature to zero-mean and unit variance for preprocessed dataset splits. Training is performed on the training split mentioned in II for about 8 h for each network. We optimize the training parameters on randomly shuffled mini-batches with Adam optimizer [48] with the learning rate $\alpha = 0.00013$. We calculate the mean squared error (MSE) of predicted wind speed ($\hat{v}_i$) and the wind speed label (v_i) across N samples as the training and validation loss, written as

$$Loss(v, \hat{v}) = \frac{\sum_{i=1}^{N}(\hat{v}_i - v_i)^2}{N}. \tag{1}$$

We employ 512 samples for each batch and validate the model with the validation split after each training epoch to avoid overfitting. Under the early-stopping condition, the validation loss determines when to stop with a patience of 6 epochs before training reaches its maximum epochs of 100. Models with the lowest validation loss will be saved for inference and further evaluation.

D. Evaluation Metrics

After training, the evaluation is performed on the unseen test split for each network. In addition to comparing the baseline and the fusion models' performances, we include wind speeds estimated by the conventional and currently operational retrieval

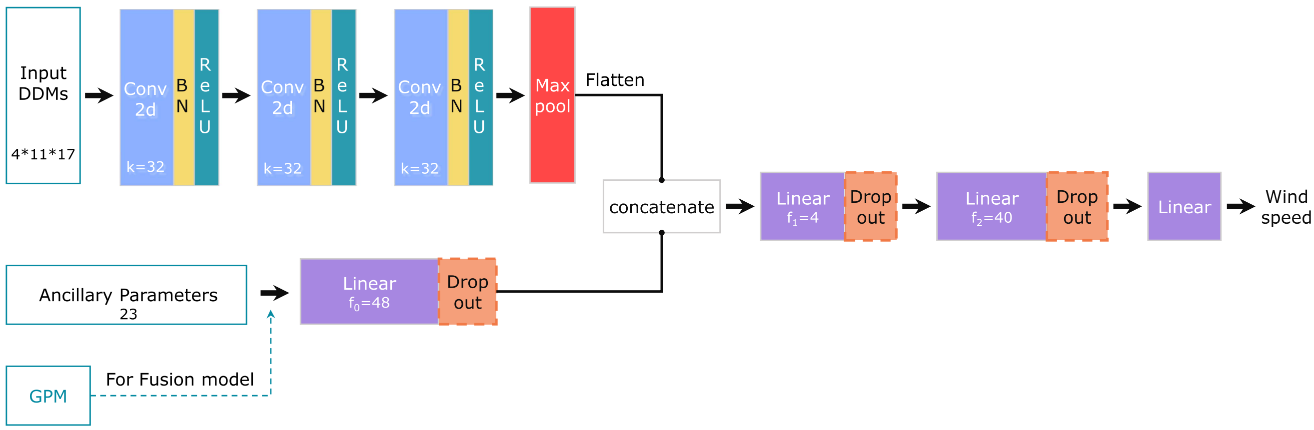

Fig. 3. Specific structure of CyGNSSnet for the experiment, modified from [24]. The map feature extractor comprises 3 convolutional layers with parameters: kernel number $k = 32$, window size $= 3 \times 3$, padding $= 1$, stride $= 1$, followed by 2-D maximum pooling with window size 2×2. The feature count is 1280 after flattening. The ancillary feature extractor incorporates a single FC layer with size $f_0 = 48$ and a dropout rate of 0.01. The target regressor consists of two FC layers, each with sizes $f_1 = 4$ (dropout rate 0.01) and $f_2 = 40$ (dropout rate 0.09), respectively.

algorithm, minimum variance estimator (MVE) [2], as the reference. MVE combines wind speed estimations derived by linear regression of the DDM-related observables (e.g., NBRCS and LES) against the ground truth wind speeds. The MVE wind speeds can be accessed from CYGNSS Level 2 Science Data Record Version 3.0 [49] free of charge. It is important to note that the wind speed derived by the MVE method is a Level 2 (L2) product, which includes an additional time-averaging process to achieve a resolution of 25 km. Therefore, we collocate the L2 dataset with our test dataset before comparing the model performance. In general, the collocated L2 dataset should achieve better accuracy than building an MVE using Level 1 (L1) observations.

The aforementioned models are evaluated by the following metrics: standard deviation of estimation errors (RMSE), bias, and the mean absolute percentage error (MAPE).

The overall RMSE between ERA5 wind speeds and wind predictions can be obtained by

$$\mathrm{RMSE}(v, \hat{v}) = \sqrt{\frac{\sum_{i=1}^{N} (\hat{v}_i - v_i)^2}{N}} \tag{2}$$

where $\hat{v}_i$ is the wind speed prediction and v_i represents the ground truth.

The overall bias averaging the difference between ERA5 wind speeds and predicted wind speeds is given as

$$\mathrm{Bias}(v, \hat{v}) = \frac{\sum_{i=1}^{N} (\hat{v}_i - v_i)}{N}. \tag{3}$$

In addition, the overall MAPE illustrating the average percentage deviation of the predicted wind speed from the ERA5 wind speed can be computed via

$$\mathrm{MAPE}(v, \hat{v}) = \frac{1}{N} \sum_{i=1}^{N} \left| \frac{\hat{v}_i - v_i}{v_i} \right| \times 100\%. \tag{4}$$

IV. Evaluation Results

In this section, we evaluate the overall performance of the baseline and fusion models over the entire test dataset of 266 days. We compare their performance under precipitation conditions and demonstrate quantitative results for different wind speed intervals. We further investigate the spatial distribution patterns of the metrics on a global scale and validate the generalization of our model in time. Finally, a case study of Hurricane Laura is performed using our fusion model to assess its effectiveness during extreme events.

A. Overall Performance

The overall RMSE, bias, and MAPE for both networks as well as MVE estimations are reported in Table IV. For all samples over 9 months in our test dataset, both deep learning-based models achieve lower RMSE than the conventional algorithm MVE. The fusion model, in particular, yields the lowest RMSE (1.28 m/s), bias (0.03 m/s), and MAPE (15.49%). The overall RMSE shows that the fusion model outperforms the baseline model by 3.3% and MVE by 30%. Moreover, the average prediction bias of the fusion model is close to 0 and is decreased by 50% compared with the baseline model. The MAPE agrees with the RMSE and bias that the fusion model performs better than the other two methods. Even though the MVE algorithm adds extra processing steps, such as time averaging, to achieve better wind speed estimates, deep learning models outperform the MVE and our CyGNSSnet fusion model reports a better estimation than the baseline model. Fig. 4 presents the probability density of wind speed estimations from three models in comparison to the wind speed distributions of the corresponding ERA5 data as the ground truth. All three models report similar shapes and match close to the ground truth, but are different in peaks.

The peak of MVE wind speed estimations lies closer to 6 m/s whereas both baseline and fusion model estimations lie close to 8 m/s, aligning better with the ground truth. The dispersion of both deep learning models as well as MVE are lower than

TABLE IV
RMSE, BIAS, AND MAPE OBTAINED ON ALL TEST SAMPLES FOR DIFFERENT MODELS AND ERA5 WIND SPEED v

Model	RMSE (m/s)	Bias (m/s)	MAPE (%)
MVE	1.83	-0.71	23.13
CyGNSSnet Baseline	1.31	0.06	15.75
CyGNSSnet Fusion	**1.28**	**0.03**	**15.49**

The bold values indicate the models with the lowest RMSE, bias, and MAPE, highlighting the best-performing model with the highest accuracy in predictions.

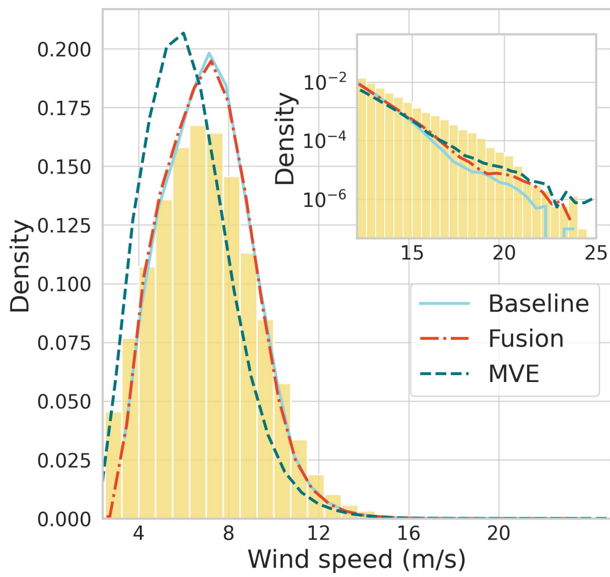

Fig. 4. PDF of MVE, baseline, and fusion model estimations (green, orange, and light blue lines) and ERA5 wind speed (yellow bar).

the ground truth with more estimations around the peak leading to a higher density compared to the ground truth wind speed between 6 m/s and 8 m/s. In the inset plot showing the higher range of wind speed, the baseline model shows notably fewer estimations, especially for wind speed exceeding 16 m/s; the fusion model matches the ground truth distribution better albeit with a slightly lower density; the tail behavior of MVE is more similar to the ground truth albeit with a slightly higher density when wind speed exceeds 25 m/s. It is evident that the fusion model improves the accuracy at high wind speed compared to the baseline and demonstrates the best overall fit but with more concentrated estimations at the mean value. The conventional MVE model, in the meantime, may have a stable performance at low wind speeds and a better alignment in the extreme range but still contains a negative bias in the majority of the estimations. The estimation distribution result shows that data fusion with precipitation information will enhance the model performance, especially at higher wind speeds.

Further, we evaluate the performance of the models in different ranges of wind speeds. Table V summarized the RMSE and bias of the models performed on different wind speed intervals. In terms of general RMSE, both models outperform the MVE wind speed, however, the MVE still performs better regarding RMSE for winds lower than 4 m/s. In the regime of low wind

TABLE V
RMSE AND BIAS OBTAINED ON ALL TEST SAMPLES WITHIN DIFFERENT WIND SPEED INTERVALS

Metric	RMSE (m/s)			Bias (m/s)		
Wind speed (v) intervals (m/s)	MVE	Baseline	Fusion	MVE	Baseline	Fusion
All	1.83	1.31	**1.28**	-0.71	0.06	**0.03**
$2.5 < v \leq 4$	**1.35**	1.44	1.41	**0.77**	1.07	1.06
$4 < v \leq 8$	1.39	1.14	**1.11**	-0.41	0.35	**0.31**
$8 < v \leq 12$	2.44	1.40	**1.39**	-1.72	**-0.64**	-0.66
$12 < v \leq 16$	4.39	2.71	**2.63**	-3.92	-2.30	**-2.19**
$16 < v \leq 20$	6.71	4.40	**3.94**	-6.47	-4.14	**-3.63**
$v > 20$	9.41	6.50	**5.87**	-9.24	-6.31	**-5.64**

The bold values indicate the models with the lowest RMSE and bias at different wind speed intervals, highlighting the best-performing model with the highest accuracy in predictions.

(v ≤4 m/s), the fusion model outperforms the baseline model by 2% in RMSE, but both models, as well as the MVE, tend to overestimate the wind speed, which may be caused by the change of scattering mechanism. At the wind speed interval of 4 m/s to 8 m/s, both models yield the minimum RMSE and the minimum absolute value of bias. Moreover, the accuracy of the predictions from the models is similar, which proves that the influence of rain is not obvious in this wind interval.

In the regime of strong winds ($v > 12$ m/s), the RMSE degrades for both models and the MVE, and the absolute value of bias increases as the training samples with higher wind speed is a small fraction in the entire dataset. Here, both models and the MVE suffered from underestimating wind speed, and the higher the true wind speed, the larger the bias of the predictions. Even in this case, the fusion model reveals a significant improvement at the wind speed within 16 m/s to 20 m/s. The RMSE is improved by 10.5% and 41.3% while bias by 24% and 47% over the baseline and the MVE, respectively. We could observe similar improvements for extreme wind speed ($v > 20$ m/s). Therefore, precipitation information fusion with the deep learning network is able to improve the quality of wind speed predictions, especially for strong winds, and will not reduce the model performance on rain-free samples.

B. Evaluation Under Precipitation Condition

As our study focuses on the correction of precipitation effects for ocean wind speed products, our evaluation is also conducted on test samples affected by rain. These test samples account for 14.9% of the unseen test split by the corresponding precipitation data, which are not used for training and validation. Table VI shows the RMSE, bias, and MAPE for both networks as well as the MVE estimations after excluding rain-free samples.

Again, the fusion model achieves the lowest RMSE and MAPE compared to the others, confirming that data fusion with precipitation information improves the wind speed prediction quality. However, we find the overall bias of the baseline model

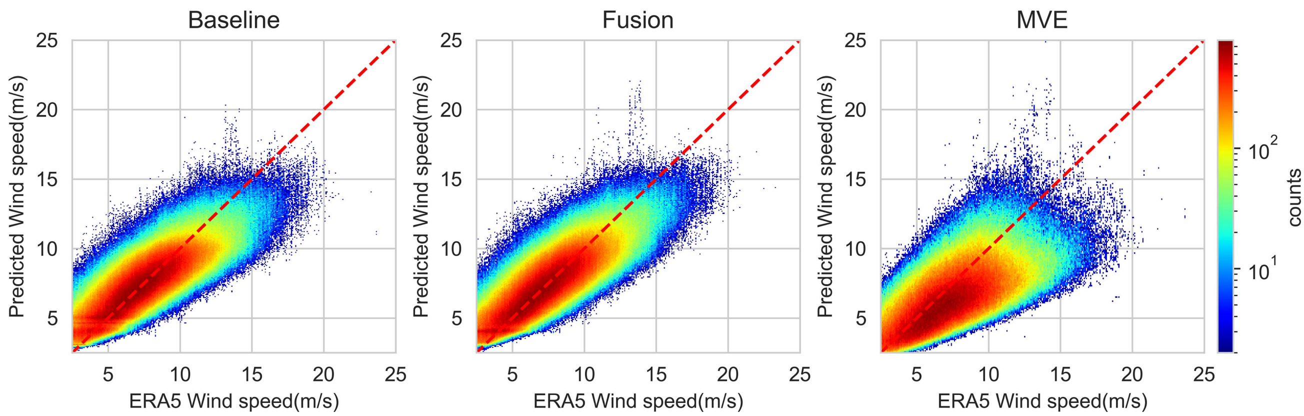

Fig. 5. Log-scale density plots of predicted wind speed over samples under precipitation conditions against the ERA5 wind speed. The left panel shows the result from the baseline model; the middle panel shows the result from the fusion model; and the right panel shows the result from MVE.

TABLE VI
RMSE, BIAS, AND MAPE FOR DIFFERENT MODELS

Model	RMSE (m/s)	Bias (m/s)	MAPE (%)
MVE	2.18	-0.77	28.20
CyGNSSnet Baseline	1.60	**0.01**	18.73
CyGNSSnet Fusion	**1.57**	0.05	**18.47**

The bold values indicate the models with the lowest RMSE, bias, and MAPE, highlighting the best-performing model with the highest accuracy in predictions.

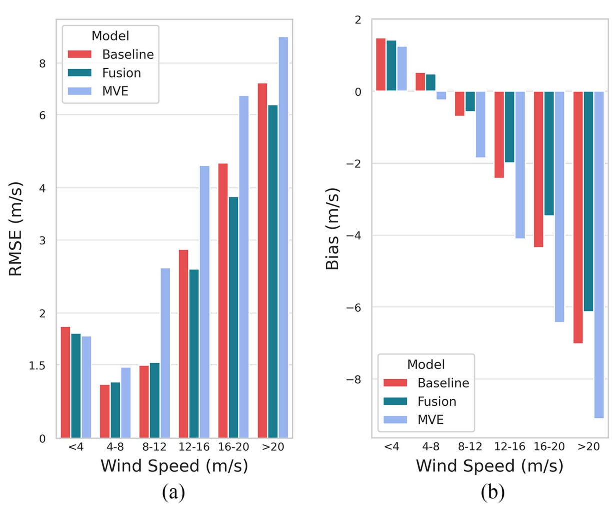

Fig. 6. RMSE (a) for different ERA5 wind speed interval and bias (b) for different ERA5 wind speed interval.

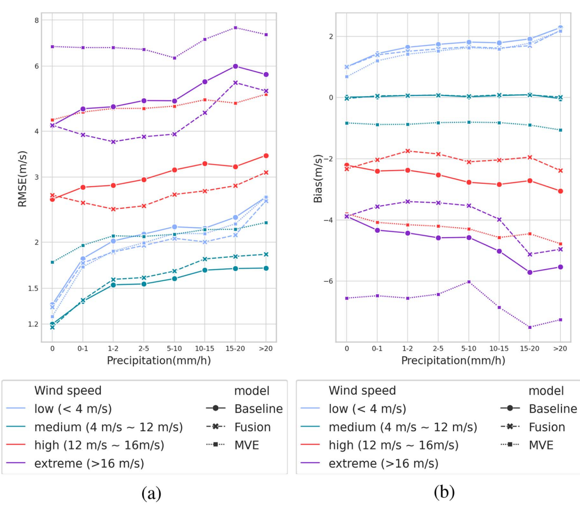

Fig. 7. RMSE for different precipitation and wind speed interval (a), bias for different precipitation and wind speed interval (b).

is smaller than that of the fusion model even if the average biases of both models are close to zero. Hence, we investigate the results by comparing the distribution of the model-predicted wind speed and the ground truth wind speed.

Fig. 5 illustrates the log-scale density plot of the ground truth wind speed labels and the predicted wind speeds for the baseline model (left), the fusion model (middle) along with those of the MVE (right) for performance comparison. Here the 1:1 line is illustrated in red, indicating the wind speed prediction is identical to the ground truth wind speed. The MVE winds spread more around the 1:1 line than the baseline and fusion model winds. Our fusion model presents the smallest dispersion, which agrees with the RMSE and bias statistics. From the baseline to the fusion model, the bump area of the density plot is reduced and more symmetrically located along the 1:1 line, verifying a much smaller standard deviation in the predictions. However, overestimation in all plots, at the wind speed of around 14 m/s is observed. Moreover, increasing underestimations at high winds ($v > 16$ m/s) are shown by both models and the MVE. Even though the differences between the plots of the baseline and fusion models are not as evident as those between the MVE, we can still observe the improvement of the predictions from the fusion model.

Fig. 6 summarizes the RMSE as well as the bias of different models in different wind speed intervals for further investigation of the model behavior. In general, all models reach a better accuracy around the second wind speed interval, and the accuracy decreases with the growth of wind speed. As shown in Fig. 6(a), the MVE achieves a higher accuracy when the wind speed is lower than 4 m/s. Better performance by the deep

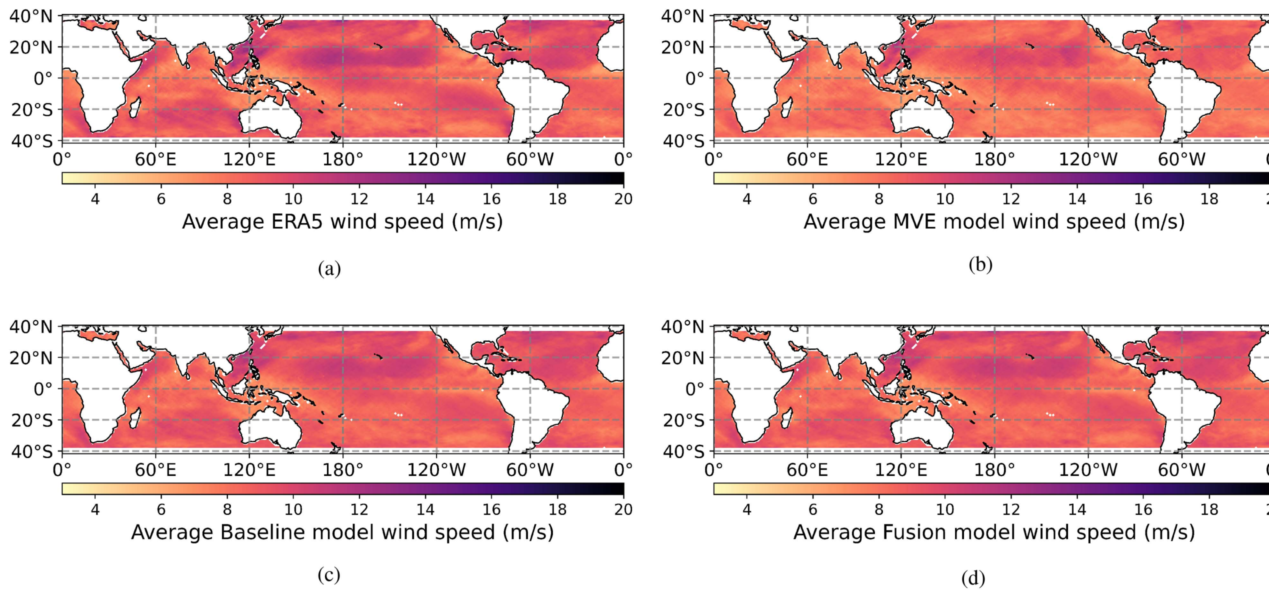

Fig. 8. Average wind speed of the (a) ERA5, (b) MVE, (c) CyGNSSnet baseline model, and (d) CyGNSSnet fusion model.

learning-based methods is obvious compared with the MVE in every other interval. Moreover, the fusion model outperforms the baseline model in both low wind speed ($v < 4$ m/s) and high wind speed ($v > 12$ m/s). Furthermore, we observe an improvement of RMSE by 17% in the challenging extreme wind speed intervals ($v > 16$ m/s) for the fusion model compared with the baseline model while the bias of which in Fig. 6(b) is decreased by 20%. All models moderately overestimate low wind speed, but the underestimation becomes larger as the wind speed grows. The MVE starts to report a negative average bias when wind speeds are larger than 4 m/s, indicating apparent underestimation among large wind speed samples. The fusion model, in contrast, outperforms the baseline and MVE models when wind speed is larger than 4 m/s with lower absolute values of the averaged bias. The improvement achieved by the fusion model is significant for retrieving high wind speed under precipitation conditions. The results agree with our assumption that using data fusion with precipitation data can correct the rain effect and improve the wind speed product quality. In addition, the RMSE and bias of different models in different wind and precipitation intervals are shown in Fig. 7. An upward trend in the RMSE can be observed in different wind speed intervals but is not as apparent as in Fig. 6, which indicates that the retrieval error increases as the precipitation goes up.

For wind speed larger than 12 m/s, the effect of rain is mainly damping. This effect suppresses the wind-generated waves and reduces the surface roughness, leading to the underestimation of retrieved wind speed [35]. Meanwhile, the effect of rain splashes, which increases the surface roughness, becomes less obvious compared to the wave generated by high wind speeds. Therefore, at high wind speed intervals, precipitation tends to suppress the ocean surface, resulting in the underestimation of wind speed. When precipitation is included as an extra parameter in the fusion model, it corrects for the damping effect so that the fusion model performs much better than the baseline model and the MVE at high wind speed ranges.

However, for wind speed between 4 m/s and 12 m/s, the baseline model achieves slightly lower RMSE, even though the biases of both models are similar. The strongly diffuse (quasi-specular) scattering at medium range wind speed is less sensitive to shorter wavelengths and, consequently, to precipitation. Furthermore, the presence of swell at this wind speed range may also diminish the effects of precipitation on the BRCS. This result is because of the strongly diffuse scattering, which is less sensitive to precipitation but could also be influenced by the swell, which can diminish the precipitation effects on the BRCS. Among the samples with wind speed smaller than 4 m/s, the MVE outperforms the other two models when precipitation is below $2\,\mathrm{mmh}^{-1}$. However, as precipitation increases, the RMSE of MVE grows faster than that of the fusion model. The fusion model becomes the best for precipitation larger than $5\,\mathrm{mmh}^{-1}$, followed by the MVE and the baseline model. As expected, the data fusion approach can correct the precipitation effects at low wind speed range. These results prove that including the precipitation data positively reduces the residuals in the predictions; hence, deep learning-based data fusion is reasonably competitive in retrieving ocean surface wind speed.

C. Geographical Analysis

Fig. 8 shows the geographical distributions of averaged wind speed estimations of different models along with ERA5 wind speed labels. Over the entire 266-day test period, wind speeds are averaged with a resolution of 1 °. The corresponding RMSE and bias of different models are shown in Fig. 9. In general, both baseline and fusion models outperform the MVE as their global trends agree better with the ground truth. As only 14.9% of the test data is affected by precipitation, the global performance of the fusion model is quite similar to the baseline model, albeit with some improvements in RMSE such as at the South Atlantic Ocean (1.7% in average) and the South East Asia region (1.5% in average). However, we still observe similar overestimated

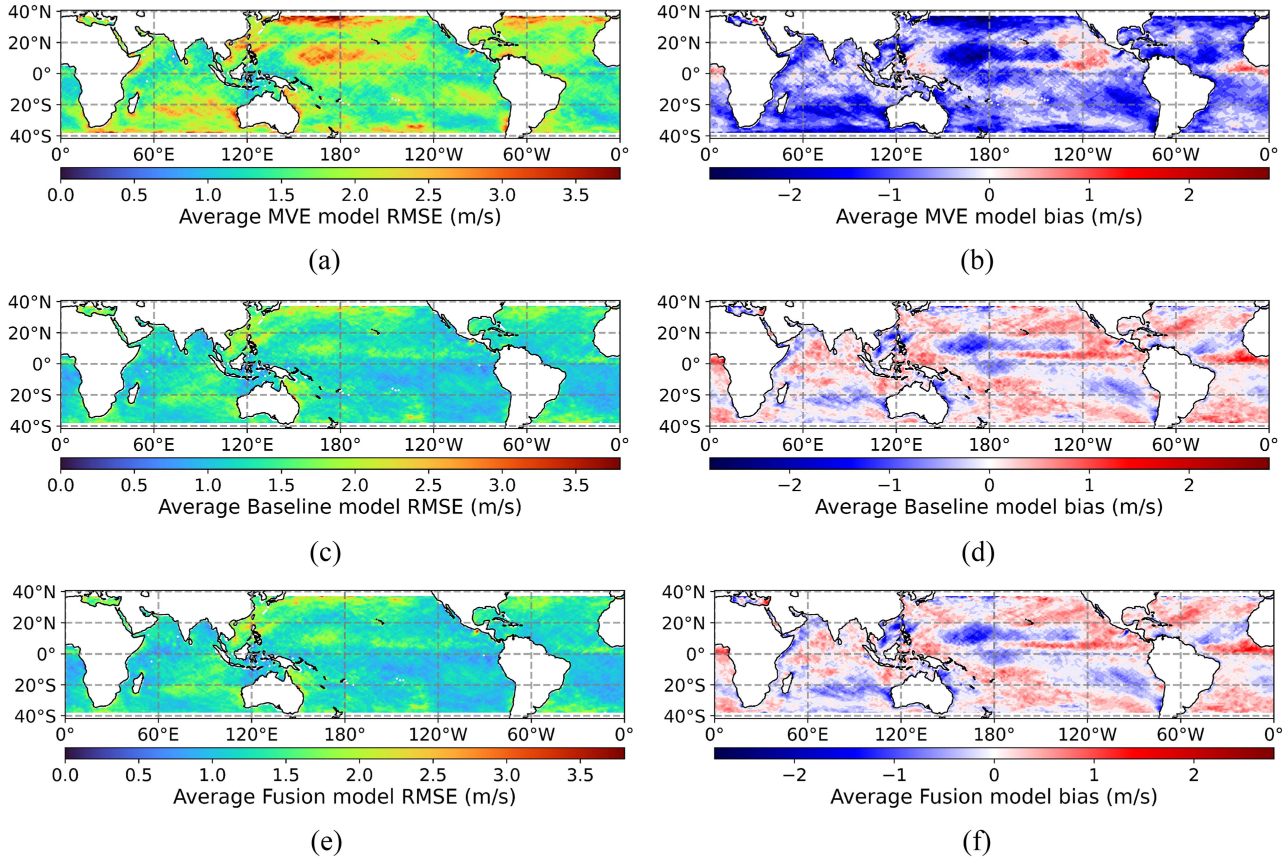

Fig. 9. RMSE (a),(c), and (e), and Bias (b), (d), and (f) of MVE, baseline, and fusion models compared with ERA5 labels.

spatial patterns in Asia-Pacific regions where the Quasi-Zenith Satellite System (QZSS) is operating. As is mentioned in [50], the radio-frequency interference (RFI) of this system leads to the degradation of the SNR of GNSS-R observations and consequently the overestimation of the retrieved wind speed. Meanwhile, we notice that all three models report overestimated wind speeds along the equator in the region spanning from longitude 80° W to 180° W. The resemblance between the overestimation patterns of different models proves that such bias was caused by neither the algorithm nor the precipitation effect but originated from the measurement. Also, the bias of different models shows some patterns with similar texture, this may related to the pattern of swell that can also alter the ocean surface roughness.

D. Generalization in Time

We assess the generalization of our model by applying the fusion model over the daily temporal segments of the test dataset. The daily and monthly average RMSE of the fusion model is illustrated in Fig. 10.

Despite some days with very few samples retaining more uncertainty, which may be caused by the filtering rules, the model demonstrated quite robust performance during the test period. Even if the temporal information is absent in our model input, for most of the days, the model maintains the average RMSE below the 2 m/s requirement of the CYGNSS mission. The RMSE could vary because of the seasonal differences and the number of available samples. Moreover, the monthly average RMSE stays even lower than 1.5 m/s.

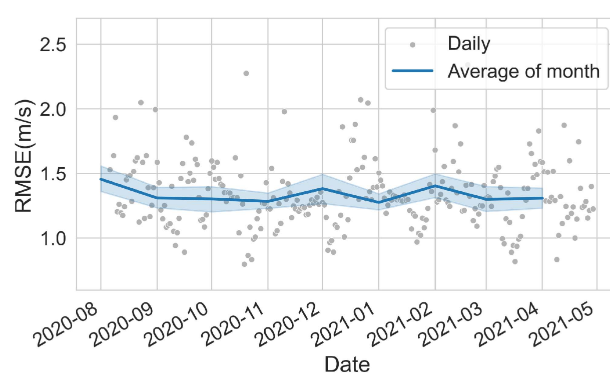

Fig. 10. RMSE of the fusion model in different time intervals of the test dataset.

E. Case Study of the Hurricane Laura

To further evaluate the reliability of the data fusion model in predicting extreme weather events, which is important for disaster response and mitigation efforts, we perform a case study of Hurricane Laura. Laura was a powerful category 4 hurricane that occurred from the 20th to the 29th of August 2020. Laura made landfall near Cameron, Louisiana, accompanied by a catastrophic storm surge of up to 18 feet above ground level on 28th August. According to the official report, the landfall

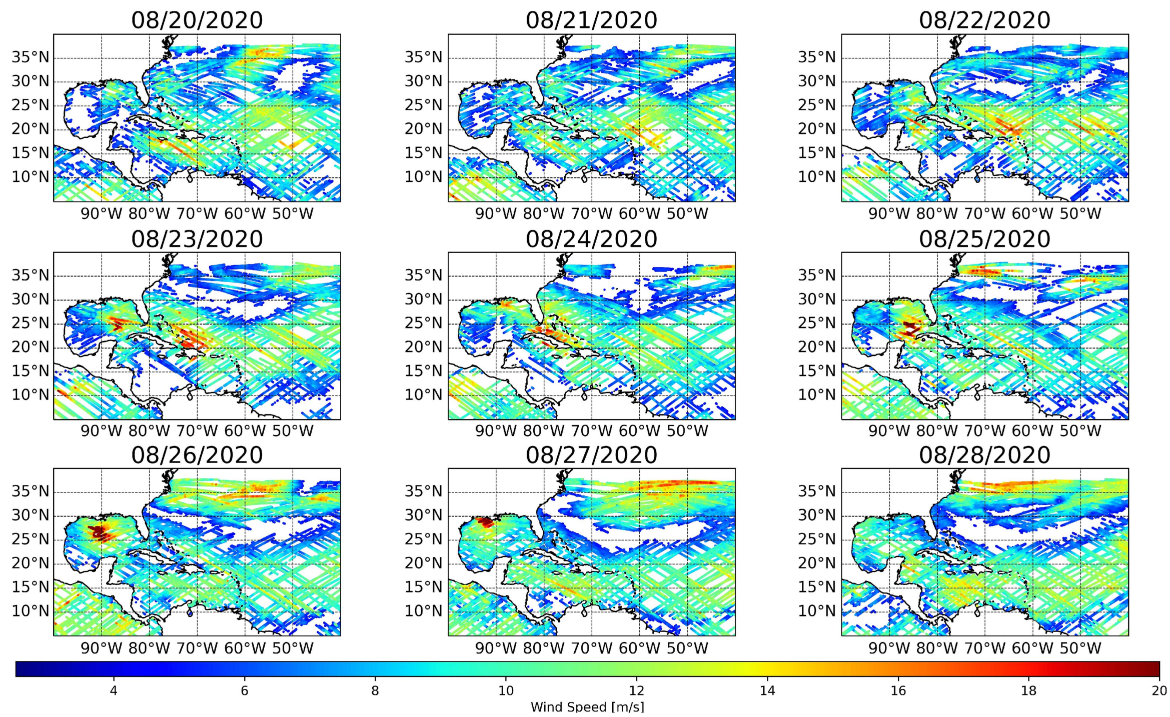

Fig. 11. Daily wind speed estimation of the study area, from 20th August to 28th August.

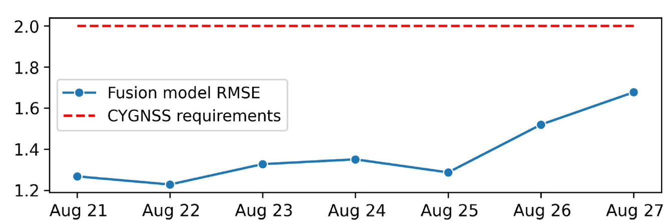

Fig. 12. Daily RMSE (m/s) of the CyGNSSnet fusion model compared with CYGNSS requirements. The observations are collected before the 28th for the case study as Laura made the landfall on 27th Aug.

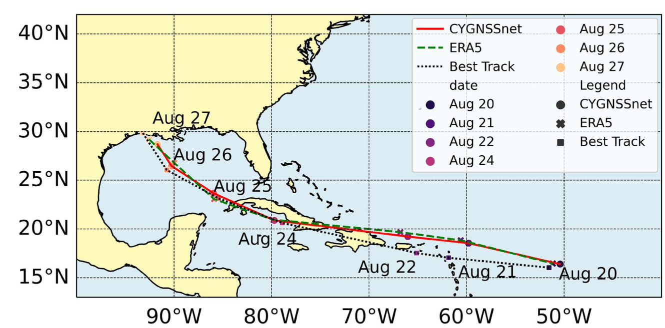

Fig. 13. Track of Hurricane Laura during the test period from 20th to 27th of August, 2020, estimated by the CyGNSSnet fusion model, the ERA5 wind speed, and Best Track recorded in the official report.

happened on the 27th of August while our focus is monitoring ocean surface wind. Thus, we collect the CYGNSS observations over the ocean in a bounding box span from 40° W to 100° W longitude and from 0° N to 40° N latitude, starting from 21st August to 27th August. The inference results of wind speeds for each day are illustrated in Fig. 11. The number of observations was reduced due to quality control, but we can still observe the cluster of extreme wind speeds locating the hurricane in the plot. Furthermore, we compared the output of our fusion model with ERA5 wind speed. The daily RMSE of our fusion model is reported in Fig. 12, showing that the overall accuracy of our fusion model fulfills the expectation of the CYGNSS mission during extreme events. Therefore, it is possible to track the hurricane over the ocean based on the wind speeds estimated by our models, which provides us with much higher temporal resolution and more information.

We estimate Laura's track over the ocean by clustering the largest estimated wind speeds of each day and comparing it with the best track location reported in the official documents [51]. It is important to note that while we select the closest time-aligned best track location for comparison, the time difference between the tracks can result in misalignment. Moreover, since the best track is constructed based on various sources of meteorological observations, whereas our estimations are only from observations over the ocean, the track may be biased if the hurricane goes through larger islands. Fig. 13 shows the estimated track of Laura calculated based on the ERA5 wind speed over the ocean, the estimated wind speed from our fusion model, and the best track in the official reports. The center of the hurricane falls over land on August 23rd so we skip the comparison of this date. It turns out that our fusion model provides a result quite near to the best track which takes in measurements from many in-situ and remote sources. Although the wind speed magnitudes are still biased, as our labels underestimate wind speed during hurricane events, our fusion model can present promising results.

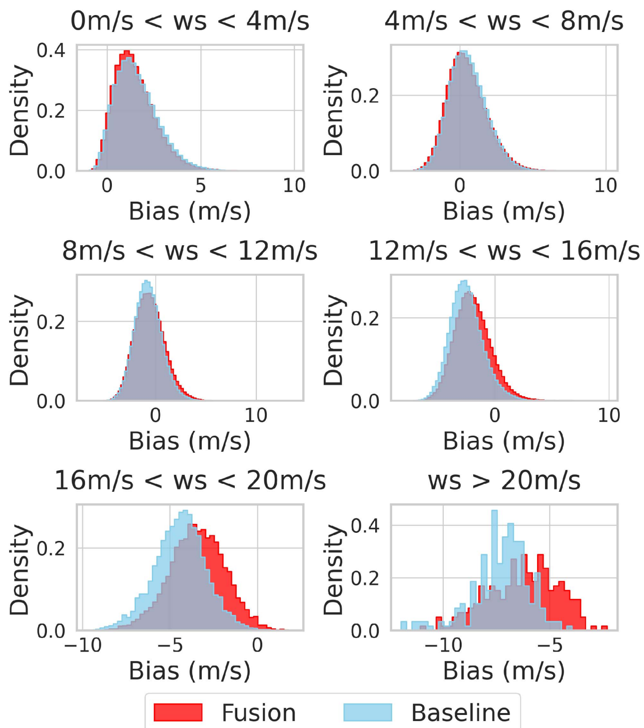

Fig. 14. Distribution of model output error (bias) in different wind speed (ws) interval.

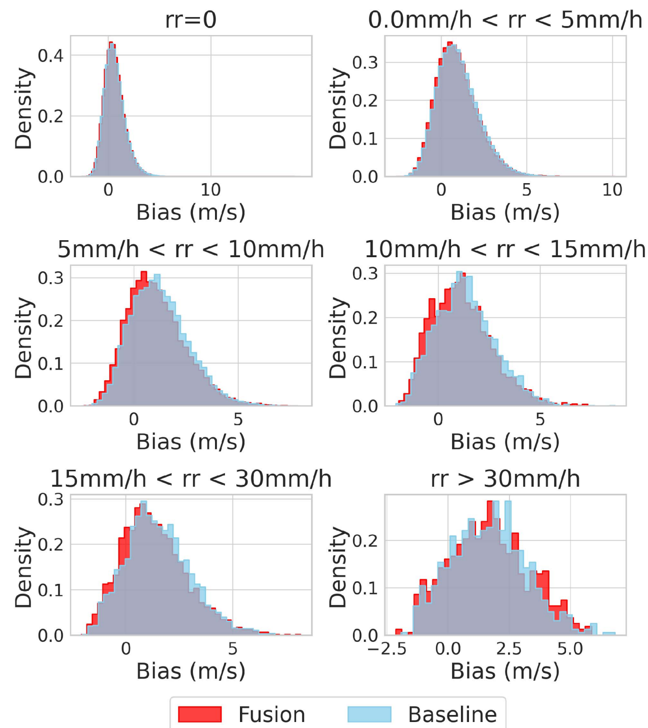

Fig. 15. Distribution of model output error (bias) in different rain rate (rr) intervals among wind speeds smaller than 6 m/s).

V. Discussion

The exploitation of deep learning for remote sensing applications is widely used and more and more of them are brought to GNSS-R. In the meantime of getting higher accuracy products, we also want to discuss how the data-driven approaches help the retrieval.

A. Precipitation Impact

Our fusion model is proven to have a better performance over the test dataset, especially under higher wind speeds. Theoretically, the raindrops will cause ring waves on the calm ocean surface that alter the surface roughness at low wind speeds. The effect of such waves becomes less obvious with the increase in wind speed, which majorly contributes to the change of surface roughness. However, Fig. 14 shows the distribution of the bias between the model predicted wind speed and the ground truth in different wind speed intervals. All samples here are influenced by the rain. Better performance is observed with lower bias when wind speed grows larger. Meanwhile, when the wind speed is lower than 4 m/s, smaller biases are reported for the fusion model.

Furthermore, we take a look into low wind speed and high wind speed intervals respectively and get the distribution of biases in different rain rate (rr) intervals. Theoretically, when surface wind speed is low, rain splashes will cause the ring wave, and the sea surface then becomes rougher. Thus, the bias will be positive and larger if the precipitation information is not considered in the model. Fig. 15 shows the distribution of model output error of low wind speed samples. Two models have similar performances when there is no precipitation ($rr = 0\,\mathrm{mmh}^{-1}$). However, we can observe that the majority of biases are positive for both models when there is precipitation. When the rain rate is smaller than $15\,\mathrm{mmh}^{-1}$, we find the bias of the fusion model is closer to the 0 line. This shows our fusion model considering precipitation information can correct the rain effect for low wind speed samples. When the rain rate is larger, the correction is limited due to the lack of training and test samples.

Moreover, we learn a much more obvious reduction of underestimation for high wind speeds Both the baseline and fusion models perform similarly when the rain rate is 0, and underestimate the wind speed. The damping effect of precipitation will reduce the height of the wave caused by surface wind and consequently bring negative biases to the wind speed estimates. The fusion model reports smaller biases for high wind speed samples under precipitation conditions. It confirms that our fusion model could notice and correct both the damping effect and ring wave effect caused by the precipitation in Fig. 16.

In addition, we look into the correlation between the wind speed and precipitation rate. We explore the data distribution of the collocated ERA5 wind speed and the precipitation rate for all samples. The density plot is shown in Fig. 17. We find that there is no significant correlation between the precipitation rate and the wind speed. The correlation coefficient of them is 0.0591. Further, we observe that the largest precipitation rates lie around moderate wind speed interval (wins speed between 6 m/s and 15 m/s) instead of extremely high wind speed range.

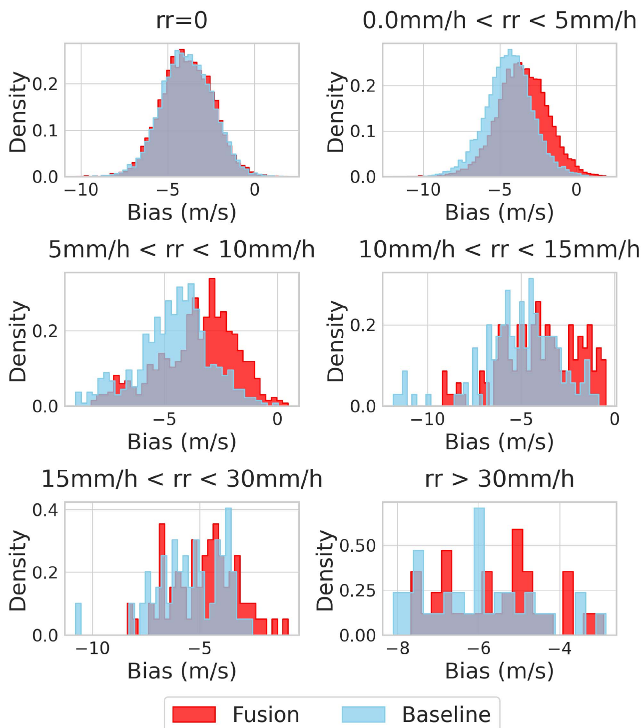

Fig. 16. Distribution of model output error (bias) in different rain rate (rr) interval among wind speeds larger than 16 m/s).

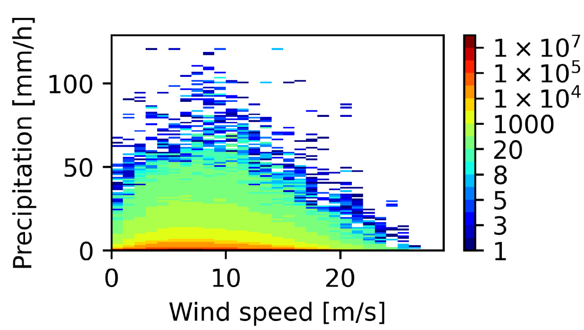

Fig. 17. Distribution of ERA5 wind speed and precipitation rate.

B. Influence of Other Input Parameters

In order to validate the selection of other ancillary parameters and DDM-like observations improves the model performance. We drop the selected features and train our two models, the baseline model and the fusion model, using the same architecture. There are four feature sets in our ablation experiment, they are described as the following.

1) Feature set #1: BRCS DDM, NBRCS, and LES. This set of features includes the parameters used for the conventional regression algorithm and the original BRCS DDM. This set of features is selected according to the previous theory and experience.
2) Feature set #2: All four DDM-like observations, NBRCS and LES. The DDM-like observations shown in Table I are used as input. The other three 2-D parameters may provide some information about the signal strength and the scattering area. NBRCS and LES are still the only parameters used as ancillary parameters.
3) Feature set #3: All 4 DDMs and all 23 selected ancillary parameters. This is our final setup for wind speed retrieval. The specific parameter names are mentioned in Table III.
4) Feature set #4: BRCS DDM, effective scattering area, and all 23 selected ancillary parameters. This set of features excludes raw and power DDMs.
5) Feature set #5: All 23 selected ancillary parameters. We remove 2-D DDM-like observations to confirm that the original DDM information is needed for more accurate estimation.

TABLE VII
MODEL PERFORMANCE OF DIFFERENT FEATURE SET

Feature set	Baseline RMSE [m/s]	Fusion RMSE [m/s]
#1: BRCS + NBRCS + LES	1.52	1.50
#2: All DDMs + NBRCS + LES	1.46	1.42
#3: All DDMs + 23 Parameters	1.31	1.28
#4: BRCS + Effective scattering area + 23 Parameters	1.33	1.32
#5: 23 Parameters	1.40	1.38

Table VII shows the RMSE of model outputs compared with the ERA5 wind speeds. We could find the improvement of adding extra DDM-like observations as model input by comparing the RMSE of feature sets #1 and #2. By comparing the results of feature sets #2 and #3, we confirm that other ancillary parameters will surely improve the model performance. Moreover, after dropping the raw counts and the analog power DDMs (feature set #4), the model performs slightly worse than the input with four DDMs. Further, with all DDM-like observations (feature set #5) excluded from the input line, the model outputs contain more errors, which means the original information is also important for retrieval. Meanwhile, the fusion model outperforms the baseline model for all feature sets. It proves that the proposed deep learning-based data fusion method could correct the rain effect and improve the quality of wind speed products.

C. Challenges

Data fusion approaches bring in new information from external data sources. It helps the model learn from such information and understand the underlying relationship between the model inputs (observations and ancillary parameters) and outputs (retrieved wind speeds). However, taking in new data always brings along with new uncertainties. In addition, there are still time differences between different datasets, which also brings uncertainties to the real precipitation value for the specific CYGNSS observation samples. As AI models are trained by the input data and the labels, the uncertainty of inputs will influence the model parameters and result in biased estimations. The slightly worse performance of the fusion model for medium wind speeds, serving as a form of compensation indicates such a drawback of data fusion. However, when compared to the significant improvement seen in other wind speed intervals, the relatively small drop in accuracy among samples near the mean wind speed is acceptable. It is not easy to eliminate such uncertainty, but reduction is possible by choosing a better data source with accurate location and time information.

Also, the empirical approaches used in this study face the same obstacles of unbalanced distribution and mislabeling. The lack of samples at the tail of the dataset brings difficulty for general fitting. New CYGNSS datasets have led to improvements in calibrations and adjusting the antenna gain pattern could contribute to more accurate estimations, especially at high wind speeds. Moreover, for data-driven algorithms, labels play the most significant role. In our study, all DDM observations and parameters from CYGNSS are related to temporal and spatial vicinity measurements of the wind speed provided by other data sources. Thus, the temporal and spatial differences between label and observable are unavoidable in practice. As the wind speeds may change rapidly in the regime of very low and extremely high ranges, mislabeling tends to occur more frequently at such ranges. Therefore, we need to be cautious when selecting and collocating training data. Additional data selection and augmentation can be helpful, but discretion is needed to avoid overfitting.

In addition, the "tendency to mean" issue of training deep learning models discussed in [24] is still a problem for training our model. It would be better to train specialized models for high wind speeds, however, it brings about a new question about how to distinguish "large wind speed" samples from the lower ones. Another possibility could be to utilize a weighted loss function instead of the MSE and the mean absolute error, but this may contrarily reduce the accuracy for the majority of the data.

Besides, the impacts of other environmental parameters, such as swell, sea age, and sea surface temperature, are also considerable in GNSS-R wind speed retrievals. The related dataset may be from the same source as the wind speed labels used for training deep learning networks. The lack of data sources could be another problem of empirical data fusion if we need to introduce less dependence between features and labels. In addition, the more external datasets are used as the model input, the more complex procedure is needed for training and running the model. Therefore, it is crucial to balance the requirement and the cost for the operational use of the deep learning model.

VI. Conclusion

Precipitation is an important factor for ocean surface wind speed retrieval using the GNSS-R technique. It affects the received reflected GNSS signal in several different ways: by forming ring waves on a calmer ocean surface; attenuating reflected signal through refraction and scattering; and dissipating the wave by its damping effect. The proposed data fusion approach is capable of correcting the impact of rain as it provides external information on precipitation for our deep learning model. The fusion model outperforms the baseline model and the operational MVE model in the general RMSE as well as the RMSE for samples under precipitation conditions. The fusion model shows a considerable improvement in the RMSE (17%) compared to the baseline model at extreme wind speeds ($v > 16$ m/s), correcting the precipitation effect.

Utilizing data fusion is an effective approach for environmental disturbance correction and contributes to higher accuracy of the product. Deep learning models can benefit from external input datasets, gaining a deeper understanding of the underlying mechanism, and will achieve enhanced performance in operational use over the unseen dataset. Therefore, data fusion with other environmental parameters, such as swell, sea age, and sea surface pressure, can also help reduce the bias in the wind speed retrievals. These potential external parameters for data fusion will be validated and evaluated in the next steps.

Deep learning is a powerful tool for analyzing large observation datasets with different dimensions. It is capable of extracting target parameters even in the absence of prior knowledge about the underlying physical mechanisms. However, the long-tailed distribution of the data and the lack of training samples at higher winds are still issues when running deep learning models. Hence, further exploration could be focused on dealing with the unbalanced dataset to enhance the accuracy at higher winds, and a better design of the loss function would be a possible direction.

Furthermore, ancillary parameters could not be eliminated for the model to align the target parameters with the observations. However, refraining from limiting the input feature numbers could lead to the curse of the dimensionality [52], resulting in increased computational complexity, reduced model efficiency, and a high risk of overfitting. Therefore, feature engineering becomes essential for the operational application of deep learning models. Features with lower impact should be removed from the model input. Exploring feature importance could be assisted by AI, and it will be another future area of study.

The proposed deep learning-based data fusion approach shows its potential to fully utilize data from various sources, especially to take the advantage of GNSS-R technique and dive deeper to explore its all possible applications. In the meantime, with the accumulation of GNSS-R data, better quality and higher temporal resolution of labels are required for a higher precision of products. In the future, with more and more GNSS-R related missions successfully coming into operation, more potential products will be available with the assistance of AI.

Acknowledgment

The datasets used in this study are available free of charge and the authors would like to thank scientific teams associated with the CYGNSS mission at NASA and the University of Michigan for providing CYGNSS data, the European Centre for Medium-Range Weather Forecasts (ECMWF) for providing the ERA5 reanalysis wind speed estimates, and the developers of IMGERG for providing the GPM precipitation data.

References

[1] A. B. Villas et al., "Integrated observations of global surface winds, currents, and waves: Requirements and challenges for the next decade," *Front. Mar. Sci.*, vol. 6, 2019, Art. no. 434339. [Online]. Available: https://www.frontiersin.org/articles/10.3389/fmars.2019.00425

[2] M. P. Clarizia, C. S. Ruf, P. Jales, and C. Gommenginger, "Spaceborne GNSS-R minimum variance wind speed estimator," *IEEE Trans. Geosci. Remote Sens.*, vol. 52, no. 11, pp. 6829–6843, Nov. 2014.

[3] E. J. Metzger, "Upper ocean sensitivity to wind forcing in the south China sea," *J. Oceanogr.*, vol. 59, no. 6, pp. 783–798, Dec. 2003.

[4] C. Gommenginger, M. Srokosz, P. Challenor, and P. Cotton, "Development and validation of altimeter wind speed algorithms using an extended collocated buoy/topex dataset," *IEEE Trans. Geosci. Remote Sens.*, vol. 40, no. 2, pp. 251–260, Feb. 2002.

[5] J. Figa-Saldaña, J. J. Wilson, E. Attema, R. Gelsthorpe, M. R. Drinkwater, and A. Stoffelen, "The advanced scatterometer (ASCAT) on the meteorological operational (MetOp) platform: A follow on for European wind scatterometers," *Can. J. Remote Sens.*, vol. 28, no. 3, pp. 404–412, 2002, doi: 10.5589/m02-035.

[6] J. Horstmann, H. Schiller, J. Schulz-Stellenfleth, and S. Lehner, "Global wind speed retrieval from SAR," *IEEE Trans. Geosci. Remote Sens.*, vol. 41, no. 10, pp. 2277–2286, Oct. 2003.

[7] D. Hauser et al., "Satellite remote sensing of surface winds, waves, and currents: Where are we now?," *Surv. Geophys.*, vol. 44, pp. 1357–1446, Mar. 2023.

[8] V. U. Zavorotny, S. Gleason, E. Cardellach, and A. Camps, "Tutorial on remote sensing using GNSS bistatic radar of opportunity," *IEEE Geosci. Remote Sens. Mag.*, vol. 2, no. 4, pp. 8–45, Dec. 2014.

[9] M. Asgarimehr, J. Wickert, and S. Reich, "TDS-1 GNSS reflectometry: Development and validation of forward scattering winds," *IEEE J. Sel. Topics Appl. Earth Observ. Remote Sens.*, vol. 11, no. 11, pp. 4534–4541, Nov. 2018.

[10] M. Asgarimehr, J. Wickert, and S. Reich, "Evaluating impact of rain attenuation on space-borne GNSS reflectometry wind speeds," *Remote Sens.*, vol. 11, no. 9, 2019, Art. no. 1048. [Online]. Available: https://www.mdpi.com/2072-4292/11/9/1048

[11] G. Foti et al., "Spaceborne GNSS reflectometry for ocean winds: First results from the U.K. TechDemoSat-1 mission," *Geophys. Res. Lett.*, vol. 42, no. 13, pp. 5435–5441, 2015. [Online]. Available: https://agupubs.onlinelibrary.wiley.com/doi/abs/10.1002/2015GL064204

[12] C. S. Ruf et al., "A new paradigm in earth environmental monitoring with the CYGNSS small satellite constellation," *Sci. Rep.*, vol. 8, no. 1, Jun. 2018, Art. no. 8782, doi: 10.1038/s41598-018-27127-4.

[13] C. Jing, X. Niu, C. Duan, F. Lu, G. Di, and X. Yang, "Sea surface wind speed retrieval from the first Chinese GNSS-R mission: Technique and preliminary results," *Remote Sens.*, vol. 11, no. 24, 2019, Art. no. 3013. [Online]. Available: https://www.mdpi.com/2072-4292/11/24/3013

[14] J. Garrison, A. Komjathy, V. Zavorotny, and S. Katzberg, "Wind speed measurement using forward scattered GPS signals," *IEEE Trans. Geosci. Remote Sens.*, vol. 40, no. 1, pp. 50–65, Jan. 2002.

[15] V. Zavorotny and A. Voronovich, "Scattering of GPS signals from the ocean with wind remote sensing application," *IEEE Trans. Geosci. Remote Sens.*, vol. 38, no. 2, pp. 951–964, Mar. 2000.

[16] J. Garrison and S. Katzberg, "Detection of ocean reflected GPS signals: Theory and experiment," in *Proc. IEEE SOUTHEASTCON*, 1997, pp. 290–294.

[17] M. P. Clarizia, C. P. Gommenginger, S. T. Gleason, M.A. Srokosz, C. Galdi, and M. Di Bisceglie, "Analysis of GNSS-R delay-Doppler maps from the U.K.-DMC satellite over the ocean," *Geophys. Res. Lett.*, vol. 36, no. 2, 2009. [Online]. Available: https://agupubs.onlinelibrary.wiley.com/doi/abs/10.1029/2008GL036292

[18] X. Zhu et al., "Deep learning in remote sensing: A comprehensive review and list of resources," *IEEE Geosci. Remote Sens. Mag.*, vol. 5, no. 4, pp. 8–36, Dec. 2017.

[19] L. Ma, Y. Liu, X. Zhang, Y. Ye, G. Yin, and B. A. Johnson, "Deep learning in remote sensing applications: A meta-analysis and review," *ISPRS J. Photogrammetry Remote Sens.*, vol. 152, pp. 166–177, 2019. [Online]. Available: https://www.sciencedirect.com/science/article/pii/S0924271619301108

[20] M. Asgarimehr, I. Zhelavskaya, G. Foti, S. Reich, and J. Wickert, "A GNSS-R geophysical model function: Machine learning for wind speed retrievals," *IEEE Geosci. Remote Sens. Lett.*, vol. 17, no. 8, pp. 1333–1337, Aug. 2020.

[21] X. Chu et al., "Multimodal deep learning for heterogeneous GNSS-R data fusion and ocean wind speed retrieval," *IEEE J. Sel. Topics Appl. Earth Observ. Remote Sens.*, vol. 13, pp. 5971–5981, 2020.

[22] J. Reynolds, M. P. Clarizia, and E. Santi, "Wind speed estimation from CYGNSS using artificial neural networks," *IEEE J. Sel. Topics Appl. Earth Observ. Remote Sens.*, vol. 13, pp. 708–716, 2020.

[23] X. Liu et al., "FA-RDN: A. hybrid neural network on GNSS-R sea surface wind speed retrieval," *Remote Sens.*, vol. 13, no. 23, 2021, Art. no. 4820. [Online]. Available: https://www.mdpi.com/2072-4292/13/23/4820

[24] M. Asgarimehr, C. Arnold, T. Weigel, C. Ruf, and J. Wickert, "GNSS reflectometry global ocean wind speed using deep learning: Development and assessment of CyGNSSnet," *Remote Sens. Environ.*, vol. 269, 2022, Art. no. 112801. [Online]. Available: https://www.sciencedirect.com/science/article/pii/S0034425721005216

[25] S. Arabi, M. Asgarimehr, M. Kada, and J. Wickert, "Hybrid CNN-LSTM deep learning for track-wise GNSS-R ocean wind speed retrieval," *Remote Sens.*, vol. 15, no. 17, 2023, Art. no. 4169. [Online]. Available: https://www.mdpi.com/2072-4292/15/17/4169

[26] D. Zhao et al., "DDM-Former: Transformer networks for GNSS reflectometry global ocean wind speed estimation," *Remote Sens. Environ.*, vol. 294, 2023, Art. no. 113629. [Online]. Available: https://www.sciencedirect.com/science/article/pii/S0034425723001803

[27] Y. Zhang, J. Yin, S. Yang, W. Meng, Y. Han, and Z. Yan, "High wind speed inversion model of CYGNSS sea surface data based on machine learning," *Remote Sens.*, vol. 13, no. 16, 2021, Art. no. 3324. [Online]. Available: https://www.mdpi.com/2072-4292/13/16/3324

[28] C. Wang, K. Yu, F. Qu, J. Bu, S. Han, and K. Zhang, "Spaceborne GNSS-R wind speed retrieval using machine learning methods," *Remote Sens.*, vol. 14, no. 14, 2022, Art. no. 3507. [Online]. Available: https://www.mdpi.com/2072-4292/14/14/3507

[29] D. E. Weissman et al., "Challenges to satellite sensors of ocean winds: Addressing precipitation effects," *J. Atmos. Ocean. Technol.*, vol. 29, no. 3, pp. 356–374, 2012. [Online]. Available: https://journals.ametsoc.org/view/journals/atot/29/3/jtech-d-11-00054_1.xml

[30] A. Ghavidel and A. Camps, "Impact of rain, swell, and surface currents on the electromagnetic bias in GNSS-Reflectometry," *IEEE J. Sel. Topics Appl. Earth Observ. Remote Sens.*, vol. 9, no. 10, pp. 4643–4649, Oct. 2016.

[31] R. Balasubramaniam and C. Ruf, "Characterization of rain impact on L-band GNSS-R ocean surface measurements," *Remote Sens. Environ.*, vol. 239, 2020, Art. no. 111607. [Online]. Available: https://www.sciencedirect.com/science/article/pii/S0034425719306273

[32] M. Asgarimehr, V. Zavorotny, J. Wickert, and S. Reich, "Can GNSS reflectometry detect precipitation over oceans?," *Geophys. Res. Lett.*, vol. 45, no. 22, pp. 12585–12592, 2018. [Online]. Available: https://agupubs.onlinelibrary.wiley.com/doi/abs/10.1029/2018GL079708

[33] S. Soisuvarn, Z. Jelenak, F. Said, P. S. Chang, and A. Egido, "The GNSS reflectometry response to the ocean surface winds and waves," *IEEE J. Sel. Topics Appl. Earth Observ. Remote Sens.*, vol. 9, no. 10, pp. 4678–4699, Oct. 2016.

[34] S. Durden and J. Vesecky, "A physical radar cross-section model for a wind-driven sea with swell," *IEEE J. Ocean. Eng.*, vol. 10, no. 4, pp. 445–451, Oct. 1985.

[35] N. J. M. Laxague and C. J. Zappa, "The impact of rain on ocean surface waves and currents," *Geophys. Res. Lett.*, vol. 47, no. 7, 2020, Art. no. e2020GL087287, doi: 10.1029/2020GL087287. [Online]. Available: https://agupubs.onlinelibrary.wiley.com/doi/abs/10.1029/2020GL087287

[36] J. Bu, K. Yu, X. Zuo, J. Ni, Y. Li, and W. Huang, "GloWS-Net: A. deep learning framework for retrieving global sea surface wind speed using spaceborne GNSS-R data," *Remote Sens.*, vol. 15, no. 3, 2023, Art. no. 590. [Online]. Available: https://www.mdpi.com/2072-4292/15/3/590

[37] J. Bu, K. Yu, F. Zhu, X. Zuo, and W. Huang, "Joint retrieval of sea surface rainfall intensity, wind speed, and wave height based on spaceborne GNSS-R: A case study of the oceans near China," *Remote Sens.*, vol. 15, no. 11, 2023, Art. no. 2757. [Online]. Available: https://www.mdpi.com/2072-4292/15/11/2757

[38] CYGNSS, "CYGNSS level 1 science data record version 3.0 netcdf data dictionary," PO. DAAC, fname USA CA. Dataset Accessed on: Oct. 6, 2021. [Online]. Available: https://archive.podaac.earthdata.nasa.gov/podaac-ops-cumulus-docs/cygnss/open/L1/docs/148-0346-8_L1_v3.0_netCDF_Data_Dictionary.xlsx

[39] A. G. Voronovich and V. U. Zavorotny, "The transition from weak to strong diffuse radar bistatic scattering from rough ocean surface," *IEEE Trans. Antennas Propag.*, vol. 65, no. 11, pp. 6029–6034, Nov. 2017.

[40] CYGNSS. 2020, "CYGNSS level 1 science data record version 3.0," PO. DAAC, USA CA. Dataset, Accessed on: Oct. 06, 2021. doi: 10.5067/CYGNS-L1X30. [Online]. Available: https://podaac.jpl.nasa.gov/dataset/CYGNSS_L1_V3.0

[41] C. Ruf et al., in *CYGNSS Handbook*, Ann Arbor, MI, USA: Univ. Michigan Press, 2016.

[42] M. P. Clarizia and C. S. Ruf, "Wind speed retrieval algorithm for the cyclone global navigation satellite system (CYGNSS) mission," *IEEE Trans. Geosci. Remote Sens.*, vol. 54, no. 8, pp. 4419–4432, Aug. 2016.
[43] G. J. Huffman, E. F. Stocker, D. T. Bolvin, E. J. Nelkin, and J. Tan, "GPM IMERG final precipitation L3 half hourly 0.1 degree× 0.1 degree V06 Greenbelt, MD, Goddard earth sciences data and information services center (GES DISC)." Accessed: Oct. 06, 2021, doi: 10.5067/GPM/IMERG/3B-HH/06.
[44] H. Hersbach et al., "ERA5 hourly data on single levels from 1940 to present," Copernicus Climate Change Service (C3S) Climate Data Store (CDS). Accessed: Dec. 11, 2023, doi: 10.24381/cds.adbb2d47.
[45] N. Srivastava, G. Hinton, A. Krizhevsky, I. Sutskever, and R. Salakhutdinov, "Dropout: A. simple way to prevent neural networks from overfitting," *J. Mach. Learn. Res.*, vol. 15, no. 56, pp. 1929–1958, 2014. [Online]. Available: http://jmlr.org/papers/v15/srivastava14a.html
[46] C. E. Nwankpa, W. Ijomah, A. Gachagan, and S. Marshall, "Activation Functions: Comparison of trends in practice and research for deep learning," in *Proc. 2nd Int. Conf. Comput. Sci. Technol.*, Jamshoro, Pakistan, 2021, pp. 124–133. [Online]. Available: https://arxiv.org/abs/1811.03378
[47] W. Falcon, and The PyTorch lightning team, "PyTorch lightning," Mar. 2019. [Online]. Available: https://github.com/Lightning-AI/lightning
[48] D. P. Kingma and J. Ba, "Adam: A method for stochastic optimization," in *Proc. 3rd Int. Conf. Learn. Representations*, San Diego, CA, USA, May 2015. [Online]. Available: https://arxiv.org/abs/1412.6980
[49] CYGNSS. 2020, "CYGNSS level 2 science data record version 3.0," PO. DAAC, USA CA. Dataset Accessed on: Oct. 03, 2021, doi: 10.5067/CYGNS-L2X30. [Online]. Available: https://podaac.jpl.nasa.gov/dataset/CYGNSS_L2_V3.0
[50] J. Querol, A. Alonso-Arroyo, R. Onrubia, D. Pascual, H. Park, and A. Camps, "SNR degradation in GNSS-R measurements under the effects of radio-frequency interference," *IEEE J. Sel. Topics Appl. Earth Observ. Remote Sens.*, vol. 9, no. 10, pp. 4865–4878, Oct. 2016.
[51] R. J. Pasch, R. Berg, D. P. Roberts, and P. P. Papin, "National hurricane center tropical cyclone report: Hurricane Laura (AL132020)," *Nat. Ocean. Atmos. Admin.*, Washington, DC, 2021. Accessed: Jan. 15, 2023. [Online]. Available: https://www.nhc.noaa.gov/data/tcr/AL132020_Laura.pdf
[52] G. Hughes, "On the mean accuracy of statistical pattern recognizers," *IEEE Trans. Inf. Theory*, vol. 14, no. 1, pp. 55–63, Jan. 1968.

Tianqi Xiao (Student Member, IEEE) received the B.E. degree in remote sensing science and technology from Wuhan University, Wuhan, China, in 2018, and the M.Sc degree in geomatics engineering from the University of Stuttgart, Stuttgart, Germany, in 2021. She is currently working toward the Ph.D. degree in deep learning and GNSS reflectometry with the German Research Centre for Geosciences, Potsdam, Germany, and the Technical University of Berlin, Berlin, Germany.

Her research interests include remote sensing and earth observation, deep learning, and GNSS reflectometry.

Caroline Arnold received the M.Sc. degree in physics from the University of Tübingen, Tübingen, Germany in 2015 and the Ph.D. degree in theoretical physics from the University of Hamburg, Hamburg, Germany, in 2019.

She joined Helmholtz AI in 2020 as an AI Consultant with the German Climate Computing Center DKRZ. Her current interests include machine learning and data science for Earth, climate, and environmental science.

Daixin Zhao received the B.E. degree in remote sensing science and technology from Wuhan University, Wuhan, China, and the M.Sc. degree in geomatics engineering in University of Stuttgart, Stuttgart, Germany, in 2014 and 2018, respectively.

He was with the Institute of Photogrammetry and Geoinformation, Leibniz University Hannover, Hannover, Germany, in 2018. He is currently pursuing the Ph.D. degree in deep learning and GNSS reflectometry at the German Aerospace Center (DLR), Weßling, Germany, and the Technical University of Munich, Munich, Germany. His research interests include remote sensing and Earth observation, deep learning, and GNSS reflectometry.

Lichao Mou received the bachelor's degree in automation from Xi'an University of Posts and Telecommunications, Xi'an, China, in 2012, the master's degree in signal and information processing from the University of Chinese Academy of Sciences, Beijing, China, in 2015, and the Dr.-Ing. degree in remote sensing from the Technical University of Munich, Munich, Germany, in 2020.

Since 2019, he has been a Research Scientist with the Remote Sensing Technology Institute, German Aerospace Center, Weßling, Germany, and an AI Consultant at the Helmholtz Artificial Intelligence Cooperation Unit. In 2015, he spent six months with the Computer Vision Group, University of Freiburg, Freiburg, Germany. In 2019, he was a Visiting Researcher with Cambridge Image Analysis Group (CIA), University of Cambridge, Cambridge, U.K. He is currently a Guest Professor with Munich AI Future Laboratory AI4EO, TUM, and the Head of the Visual Learning and Reasoning Team, Department EO Data Science, IMF, DLR.

Dr. Mou was a recipient of the First Prize in the 2016 IEEE GRSS Data Fusion Contest and a finalist for the Best Student Paper Award at the 2017 Joint Urban Remote Sensing Event and the 2019 Joint Urban Remote Sensing Event.

Jens Wickert received the Diploma degree in physics from Technical University Dresden, Dresden, Germany, in 1989 and the Ph.D. degree in geophysics/meteorology from Karl-Franzens University Graz, Graz, Austria, in 2002.

He holds a joint Professorship on Global Navigation Satellite System Remote Sensing, Navigation, and Positioning of the German Research Centre for Geosciences GFZ and Technische Universität Berlin. He is also GFZ Section Head Space Geodetic Techniques and the GFZ Director on "Atmosphere on Global Change" research. He was Principal Investigator of the pioneering GPS Radio Occultation experiment aboard the German Challenging Mini-satellite Payload and also the Chair of the Science Advisory Group of the GNSS REflectometry, Radio Occultation, and Scatterometry experiment onboard the International Space Station for GNSS reflectometry and radio occultation. He has authored/coauthored more than 300 ISI listed publications on GNSS Earth observation and received several research awards.

Milad Asgarimehr is the Principal Investigator of the AI for GNSS-R (AI4GNSSR) project at the German Research Centre for Geosciences (GFZ) from the Technische Universität Berlin. He began his research at GFZ and Technische Universität Berlin in 2017 after being awarded a Ph.D. Fellowship by Geo.X, the geoscientific competence network in Berlin and Potsdam. His Ph.D. research focused on spaceborne GNSS Reflectometry and remote sensing. His work earned him the Bernd Rendel Prize from the German Research Foundation in 2020, and he successfully defended his Ph.D. that same year with the highest distinction. Currently, he is a visiting Researcher at Universitat Politècnica de Catalunya in Barcelona and collaborates remotely with the Massachusetts Institute of Technology as a DAAD PRIME (Postdoctoral Researchers International Mobility Experience) Fellow. His current research interests include integrating GNSS remote sensing with artificial intelligence for Earth system modeling by combining data from various sources and sensors.